International Journal of Material Forming (2021) 14:677–689
https://doi.org/10.1007/s12289-020-01556-x

ORIGINAL RESEARCH

A modified Johnson-Cook model of AA6061-O aluminum alloy with quasi-static pre-strain at high strain rates

Shuaishuai Yang[1] · Liqiang Sun[2] · Huakun Deng[1] · Guangyao Li[1] · Junjia Cui[1]

Received: 22 May 2019 / Revised: 18 March 2020 / Accepted: 25 March 2020 / Published online: 20 April 2020

Abstract

In this paper, specimens were first pre-stretched to different pre-strain coefficients (0, 0.4 and 0.8) under quasi-static tensile for AA6061-O aluminum alloy. Then, the specimens with different pre-strain coefficients were stretched by a high-speed tensile machine (HTM) at different strain rates (200 s^{-1}, 400 s^{-1} and 600 s^{-1}). Digital image correlation (DIC) technique was employed to measure the strains. The results showed that the yield ratio increased significantly with the pre-strain increased. As the pre-strain coefficient increased, high-speed tensile strain limitation decreased and the total tensile strain limitation increased. A modified Johnson-Cook (JC) model considering pre-strain coefficient was proposed. Numerical simulations were performed using LS-DYNA with the modified JC model. The strain field of the specimen taken by the camera agreed well with the simulated strain field.

Keywords Modified Johnson-Cook model · High strain rate · Quasi-static pre-strain · AA6061-O

1. Introduction

Aluminum alloys have enormous industrial applications due to high strength to weight ratio, good corrosion resistance, and recycling potential. However, formability of aluminum alloys was much lower than steels at room temperature which became an urgent problem for aluminum forming process. Seth et al. [1] proved that at room temperature, the sheet forming limit could be significantly increased when the sheet material was subjected to extremely high deformation speeds. Majid Zia et al. [2] investigated the formability of aluminum sheets at elevated temperatures by warm electrohydraulic high-speed forming process. Significant increases in failure strain were found. Huijuan Ma et al. [3] demonstrated that the uniform strain and fracture strain augmented with increasing expansion velocity during electromagnetic ring expansion tests.

However, it was difficult to use high speed forming method to directly form a sheet into a desired shape. Electromagnetically assisted sheet metal stamping (EMAS) was promising for industrializing. It could significantly improve the forming limit of aluminum alloy, while part shape fitness was comparable to traditional process. Guangyao Li et al. [4] studied the formability of AA5182 aluminum alloy by quasi-static-dynamic tensile test, and the test results showed that finial elongation of combined quasi-static-dynamic tensile specimens was larger than pure dynamic specimens. M.K. Choi et al. [5] developed a combined deep drawing and electromagnetic sharp edge forming to improve the formability. Jinxiu Fang. [6] et al. proposed a three-step stretching EMAS method. This method could increase the tensile depth of the 5052-T aluminum alloy by more than two times than that of quasi-static stretching. Jianhui Shang et al. [7] performed stamping experiments on 6111-T4 aluminum alloys using the EMAS techniques. The experimental results showed that this method could make the draw depth of the sheet from 44 mm to 63.5 mm compared with the traditional stamping technology without relying on lubrication. J. Imbert and M. Worswick [8] pointed out that the

- Specimens of AA6061-O aluminum alloy with different pre-strain coefficientshave been tested at different high speeds.
- A modified Johnson-Cook model containing pre-strain coefficients (λ) waspropposed. The expression of constitutive model is $\sigma = [A + F(B) \cdot \varepsilon^n][1 + F(C) \cdot \ln \dot{\varepsilon}^*][1 + F(D) \cdot \ln(1 + \lambda)]$.
- The modified JC model was verified by finite element analysis and experiment.

✉ Junjia Cui
cuijunjia@hnu.edu.cn

[1] State Key Laboratory of Advanced Design and Manufacturing for Vehicle Body, Hunan University, 410082 Changsha, China

[2] Capital Aerospace Machinery Company, 100076 Beijing, China

20 mm part radius pre-formed by conventional stamping could be reduced to 5 mm using a specially designed coil. It could be seen that the EMAS method had great advantages in the molding process. However, the development of EMAS was more complicated and process parameters need to be carefully designed, which required designers to have in-depth research on process development. In order to simplify process development and improve the efficiency of process development, the finite element analysis (FEA) method was used for the simulation work of EMAS.

FEA simulation played an important role in predicting sheet metal forming, reducing product processing and increasing production efficiency. Many researchers had conducted EMAS analysis by means of FEA simulation [9–11]. In order to establish an accurate finite element model, it was essential to build an accurate constitutive model [12–14]. There were many constitutive models that were widely used to describe the relationship between the flow stress and strain [15, 16]. Amir Etaati et al. [17] did a series of thermal compression experiments. The constitutive equation was modified to describe the flow behavior of materials. The very good agreement between the experimental results and predicted results indicated that the constitutive equations could be used for predicting the thermal compression deformation behavior of materials. Joost Van Slycken et al. [18] studied the mechanical properties of four different TRIP steels under high strain rate conditions. Three constitutive models for describing the complex material behavior of TRIP-steels were used. The results showed that the JC model could better reflect the behavior of materials. The JC model could clearly express work hardening, strain rate hardening, and temperature softening effect. Therefore, in many constitutive model studies and simulation software, JC model was widely used [19–21]. However, the JC model might deviate from the experimental results for different materials under different conditions. Many researchers had improved the JC model according to different materials and different experimental conditions to make the JC model fitted the experimental data very well [22–24]. Most previous studies were single tensile constitutive models, but a few studies focused on constitutive models considering pre-strain. In the quasi-static-high-speed composite forming process, different regions have different quasi-static deformation in the quasi-static forming stage. For example, in reference [5], there were different quasi-static deformations in the fillet region. And then different quasi-static deformations in the high-speed forming stage corresponded to different constitutive models. Therefore, the accuracy of the simulation is determined by the accuracy of the constitutive model.

In this study, the original specimens were firstly stretched for different lengths by means of quasi-static stretching. Then, original specimens and pre-strain specimens were stretched at different strain rates by Zwick/Roell HTM 5020 tester. The high-speed tensile tests processes of specimens were photographed by a high-speed camera and strains field were calculated by DIC system. Then the JC model and modified JC model were established to describe the flow behavior over a certain range of strain rate.

2. Experiments

2.1 Materials and specimen preparation

The materials were commercial AA6061-O aluminum alloy sheets which were cold rolled to 1.2 mm thickness. The sketch size of the specimen and quasi-static tensile stress-strain curve were shown in Fig. 1. The tensile direction of all tensile specimens was the sheet rolling direction. The length of the gauge area was 25 mm and the width was 10 mm. The quasi-static specimens were stretched by an Instron 5985 universal tester with a nominal tensile strain rate of 0.001 s^{-1}.

Specimens were pre-stretched to 0%, 40%, 80% of plastic strain through an Instron 5985 universal tester at the tensile speed of 1.5 mm/s. Considering the elastic deformation of the material, the target pre-strain was presented by Eq. 1.

$$\varepsilon_p = (\varepsilon_a - \varepsilon_e)\lambda + \varepsilon_e \tag{1}$$

Where ϵ_a is the experiment ultimate tensile strain, ϵ_e is the initial elastic strain, λ is the target pre-strain coefficient, and ϵ_p is the target pre-strain. According to the stress-strain curve showed in Fig. 1, the initial elastic strain and ultimate strain were 0.006 and 0.2647, respectively. According to the experimental design, the pre-strain coefficients were equal to 0, 0.4 and 0.8 respectively. Pre-strain coefficients of 0, 0.4 and 0.8 represented pre-strains of 0, 0.109 and 0.213, respectively. Hence, pre-stretched distances were determined as 0 mm, 2.879 mm, and 5.935 mm.

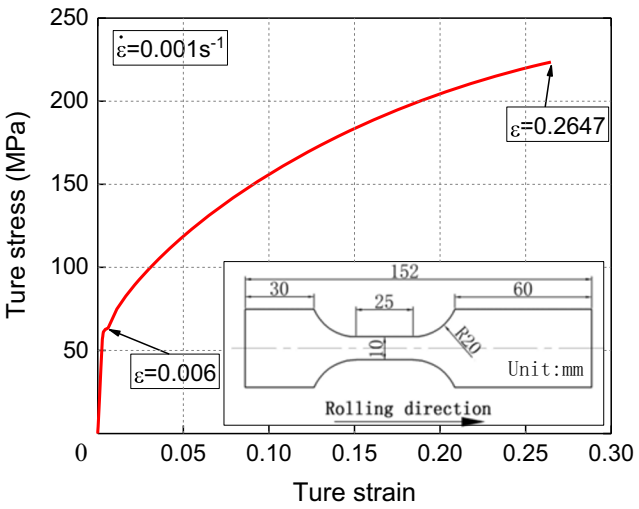

Fig. 1 Tensile testing results under quasi-static condition

2.2 Experimental procedures

The prepared specimens with different pre-strain coefficients (0, 0.4 and 0.8) were stretched at different strain rates (200 s^{-1}, 400 s^{-1} and 600 s^{-1}). High speed tensile tests were employed by HTM, and the whole processes of specimens were photographed by a camera with DIC system. The experimental process was shown in Fig. 2.

In order to capture the strain data during plastic deformation with the DIC camera, the suitable speckle points were spotted on the surface of the specimens by a speckle making tool. After speckle points were spotted, the specimens were clamped on the high-speed tensile machine. The lower grip of the high-speed tensile machine was embedded with a piezoelectric sensor used to collect the force of the test specimens during the experiment. Before the experiment begin, the high-speed tensile machine would be pre-loaded at a speed of 0.1 mm per minute and the peak pre-load force was 400 N (less than the yield strength of the specimen), which was to eliminate the clamping gap or the residual force during the clamping process. The HTM took the hydraulic accumulator as the power source and the stability of the tension speed was ensured by adjusting the size of the hydraulic valve. The DIC camera was triggered by the HTM. In the high-speed tensile experiment, the DIC camera transmitted the captured photos to the DIC operation platform via the network cable. Different tensile speeds corresponded to different frame rate and pixel resolution (taking the tensile speed of 15 m/s as an example, the frame rate and the pixel resolution of the cameras were 10000 frames/s and 384 × 264, respectively). The camera controlled the acquisitive frequency of the DAQ acquisition card. The load signal collected by the DAQ acquisition card was input to the DIC operation platform.

The DIC camera was used to record the deformation process of the test piece, and the data such as strain and displacement of the test piece could be calculated [25, 26]. The DIC operating platform was used to process photos taken by the camera. During the stretching of the specimen, the high-speed camera could capture the entire deformation process of the specimen. Through the calculation of the DIC software, the strain field in the gauge area of the specimen could be obtained. The strain at any point in the gauge area could be obtained. In this paper, the center position point in the gauge area was selected as the measurement strain point. The required engineering strain was the strain on the longitudinal direction (tensile direction) of the specimens, and the longitudinal strain of the specimens corresponded to the longitudinal strain (e_{yy}) in the software. The strain after neck was not considered.

When the pre-strain coefficient was equal to 0, the center position point in the gauge area was selected as the measurement strain point. The e_{yy} of the measuring point was the engineering strain, as shown in Eq. 2. The ratio of the force collected by the HTM to the initial cross-sectional area of the specimen was considered to be engineering stress, as shown in Eq. 3. Engineering stresses and engineering strains were transformed into true stresses and true strains by Eq. 4 and Eq. 5.

$$\varepsilon_p = e_{yy} \tag{2}$$

$$\sigma_e = \frac{F}{A_0} \tag{3}$$

$$\varepsilon_t = ln(1 + \varepsilon_e) \tag{4}$$

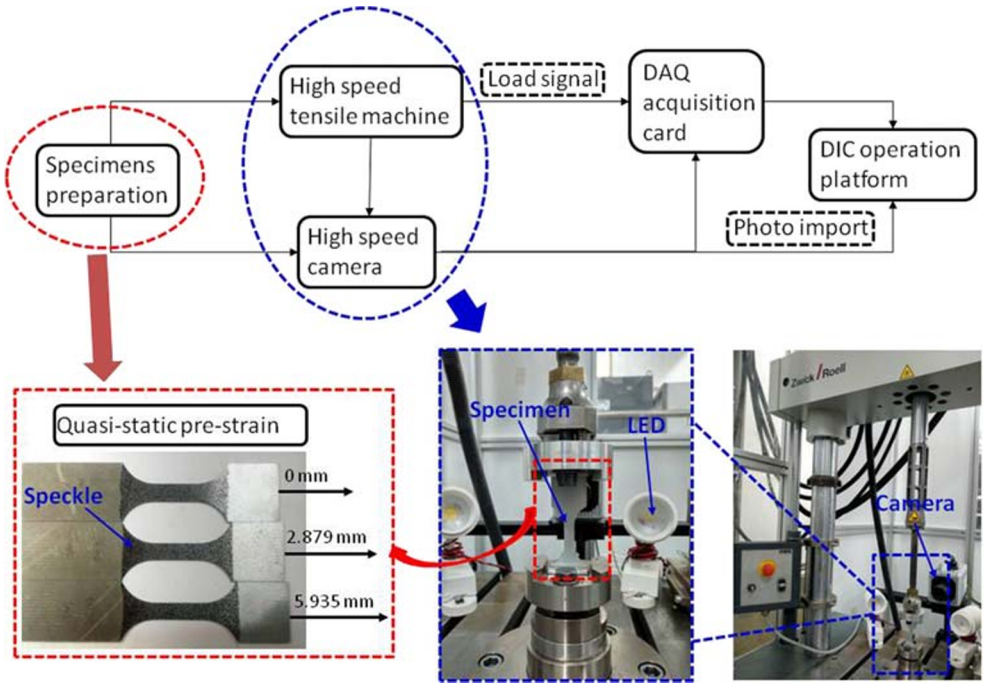

Fig. 2 The process of high-speed tensile tests

$$\sigma_t = \sigma_e \cdot (1 + \varepsilon_e) \tag{5}$$

Where ϵ_e is engineering strain, σ_e is engineering stress, A_0 is the original cross-sectional area of the gauge area, ϵ_t is true strain, σ_t is true stress.

When the pre-strain coefficient was equal to 0.4 or 0.8, engineering strain was also the e_{yy} value of the center position point in the gauge area. Before the neck of the specimen, the deformation in the gauge region was considered to be uniform [27]. Even when the pre-strain coefficient was 0.8, the test specimen had not reached the neck. When the pre-strain coefficient was equal to 0.4 or 0.8, the principle of volume constancy in the gauge area was used. This principle was presented by Eq. 6.

$$V = A_0 \cdot L_0 = A_{pre} \cdot L_{pre} \tag{6}$$

where V is the volume of the original gauge area, A_0 and L_0 are the original cross-sectional area and length of the gauge area, respectively, A_{pre} and L_{pre} are the cross-sectional area and length of the gauge area after pre-stretching, respectively. Similarly, the engineering stress after pre-stretching was the ratio of the force collected by the HTM to the cross-sectional area (A_{pre}). Therefore, the true stress-strain curve containing the pre-strain could be obtained.

3. Results and discussions

3.1 Experimental results

Specimens with different pre-strain coefficients were stretched at different strain rates. The result of stress-strain curves was shown in Fig. 3.

The yield strength and tensile strength versus pre-strain coefficient graph was shown in Fig. 4(a). As the pre-strain coefficient increased, the value of yield strength exhibited a significant increase in nonlinearity, which was due to the strengthening of the material caused by quasi-static pre-strain. In contrast to the yield strength, the tensile strength showed a nearly linear increase.

Yield ratio were shown Fig. 4(b) under different pre-strain coefficients. When the pre-strain coefficient was 0, the yield ratio of strain rate at 600 s^{-1} was 0.0329 higher than that of strain rate at 200 s^{-1}. Similarly, when the pre-strain coefficients were 0.4 and 0.8, the yield-strength ratios of strain rate at 600 s^{-1} were 0.0202 and 0.0324 higher than that of strain rate at 200 s^{-1}. It could be concluded that the strain rate had a little effect on the yield ratio under same pre-strain coefficient. When the strain rate was 200 s^{-1}, the yield ratio with a pre-strain coefficient of 0.8 was increased by 90.1% than the yield ratio with a pre-strain coefficient of 0. Similarly, when the strain rates were 400 s^{-1} and 600 s^{-1}, the yield ratios increased by 83.7% and 83.1%, respectively. Therefore, pre-strain could significantly increase the yield ratio of the material, which showed that the plasticity of that material deteriorated with increasing pre-strain coefficient.

When the pre-strain coefficients of the specimens were not zero, the total tensile true strains of the specimens included two parts: quasi-static pre-stretched true strain and high-speed tensile true strain. Pre-stretched true strain, high-speed tensile true strain and total true strain were defined as:

$$\varepsilon_q = \int_{L_0}^{L_1} \frac{dL}{L} = \ln \frac{L_1}{L_0} \tag{7}$$

$$\varepsilon_h = \int_{L_1}^{L_2} \frac{dL}{L} = \ln \frac{L_2}{L_1} \tag{8}$$

$$\varepsilon_f = \int_{L_0}^{L_2} \frac{dL}{L} = \ln \frac{L_2}{L_0} \tag{9}$$

Where L_0, L_1 and L_2 are the length of the original specimen, the specimen after pre-stretching and the specimen before necking, respectively. According to the logarithmic method, the total true strain (ϵ_f) is equal to the sum of quasi-static pre-stretched true strain (ϵ_q) and high-speed tensile true strain (ϵ_h). The relationships between total true strain and true stress were shown in Fig. 5. It could be seen that the true stress of specimens with different pre-strain coefficients was approximately equal to the true stress without pre-stretched specimens under the same strain.

According to the material tensile curves, high-speed tensile strain limitation versus strain rate for different pre-strain coefficients was shown in Fig. 6. It could be observed that when the pre-strain coefficient was 0, the high-speed tensile strain limitation of AA6061-O aluminum alloy increased with the increased of strain rate. Similarly, when the pre-strain coefficients were 0.4 and 0.8, the same rules were also presented.

When the pre-strain coefficient was zero, the total tensile strain limitation was equal to the high-speed tensile strain limitation. When the pre-strain was not zero, the total tensile strain limitation was equal to the quasi-static pre-stretched strain plus the high-speed tensile strain limitation. Results were shown in Fig. 7. For example, at a strain rate of 200 s^{-1}, the total tensile strain limitation with a pre-strain coefficient of 0.8 was 35.9% greater than the total tensile strain limitation with a pre-strain coefficient of 0. Similarly, when the strain rates were 400 s^{-1} and 600 s^{-1}, the total tensile strain limitation with a pre-strain coefficient of 0.8 were 24.1% and 23.4% higher than the total tensile strain limitation with a pre-strain coefficient of 0. The experiment results showed that the high-speed tensile strain limitation decreased with the increase of pre-strain coefficient, but the total tensile strain limitation increased with the increased of pre-strain coefficient. The total tensile strain limitation with quasi-static pre-strain was larger than that of pure high-speed strain, which meant that quasi-

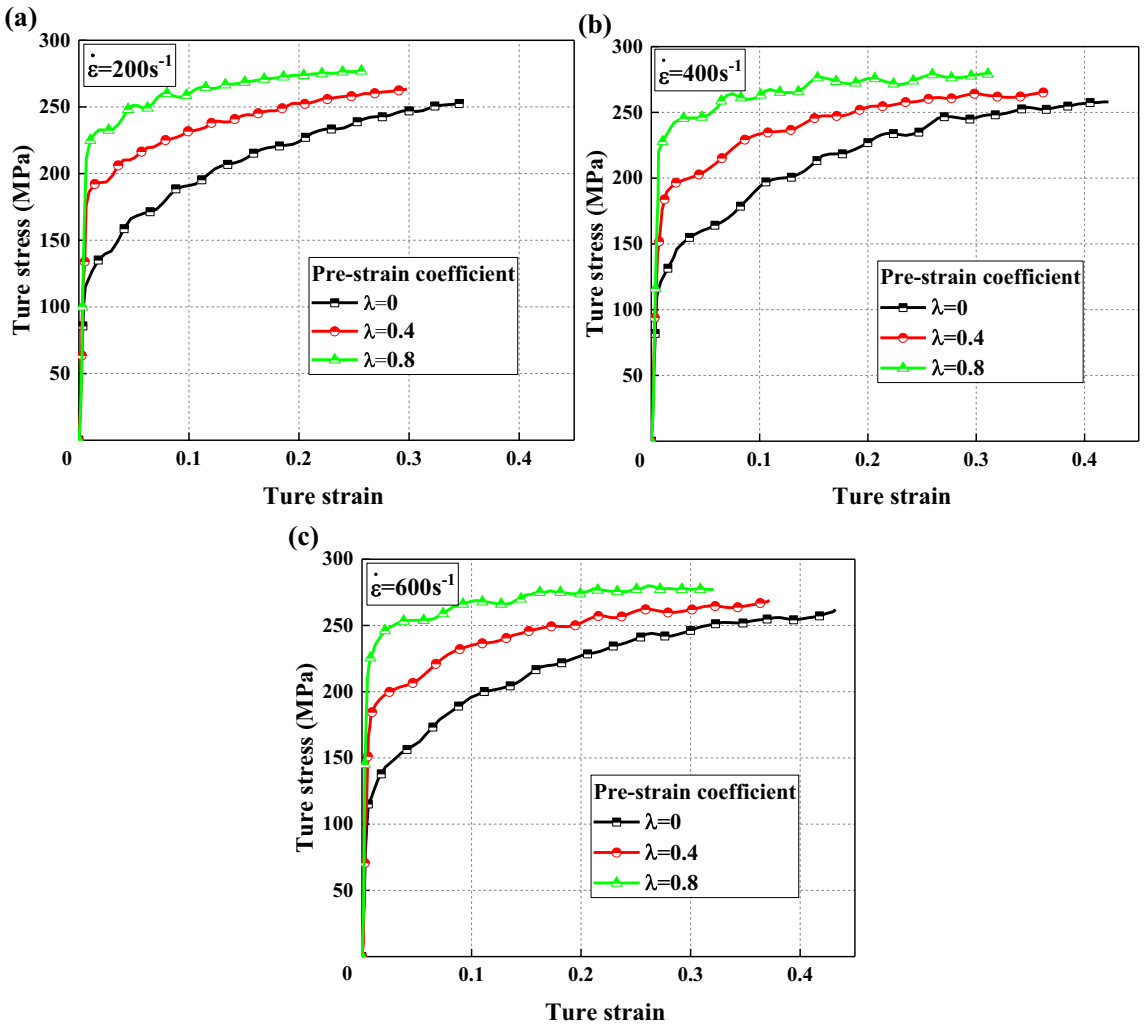

Fig. 3 True stress-true strain curves under pre-strain coefficients: (**a**) $\dot{\epsilon} = 200\ s^{-1}$, (**b**) $\dot{\epsilon} = 400\ s^{-1}$, (**c**) $\dot{\epsilon} = 600\ s^{-1}$

static-high-speed forming could improve the forming limit of materials.

Metallographic observations were conducted. The plane of the microscopic observation area was perpendicular to the thickness direction of the aluminum alloy sheet. The

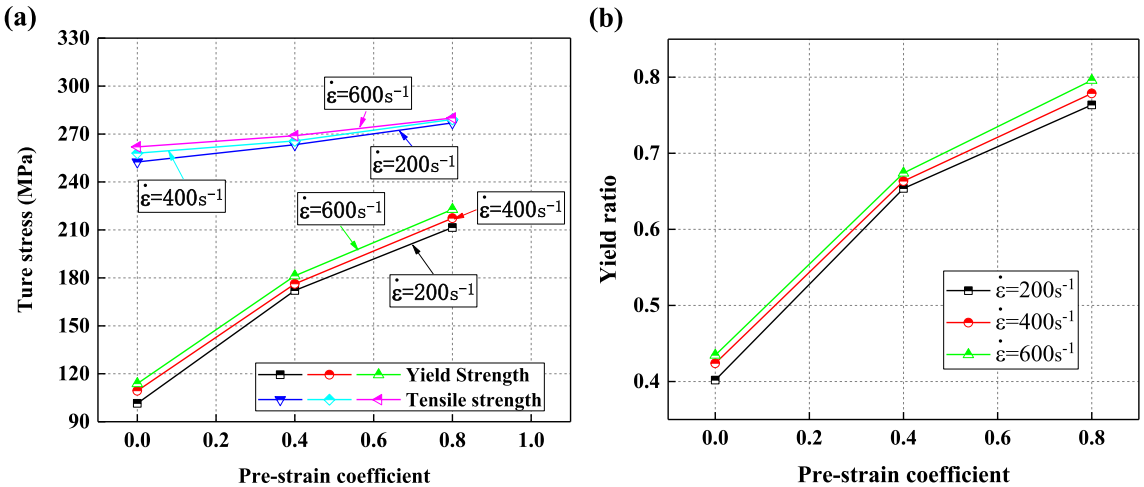

Fig. 4 Yield strength, tensile strength and yield ratio under different pre-strain coefficients: (**a**) yield strength and tensile strength versus pre-strain coefficient, (**b**) yield ratio versus pre-strain coefficient

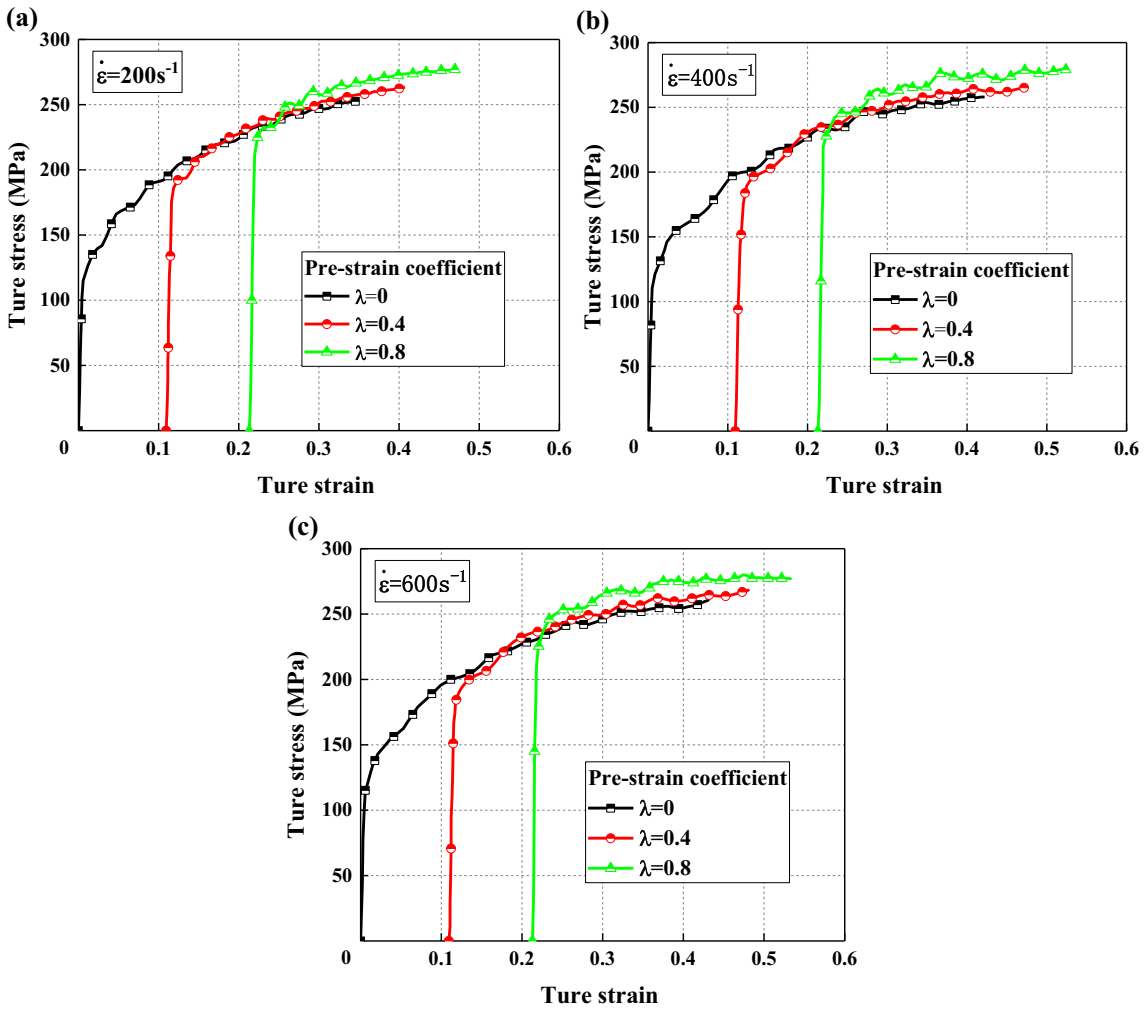

Fig. 5 True stress-total true strain curves under different pre-strain coefficients: (**a**) $\dot{\epsilon} = 200\ s^{-1}$, (**b**) $\dot{\epsilon} = 400\ s^{-1}$, (**c**) $\dot{\epsilon} = 600\ s^{-1}$

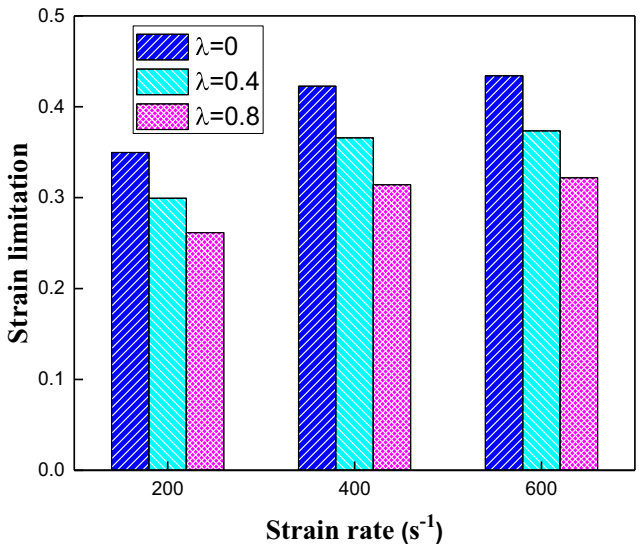

Fig. 6 Strain limitation versus strain rate at different pre-strain coefficients

observation area of the broken test piece was near the cracking position. Results were showed in Fig. 8. As could be seen in Fig. 8(a), the grain size distribution was relatively uniform and the average grain size was $15.23 \pm 7.1\ \mu m$.Cracked specimens made from high-speed stretching with 0.8 pre-strain coefficient had significantly more elongated grains than that of pure high-speed stretching condition. The result was also consistent with the conclusion that total tensile strain limitation with quasi-static pre-strain was larger than that of pure high-speed strain.

3.2 Johnson-Cook model

The JC model clearly expressed the relationship between flow stress and strain at high strain rates. The original constitutive model was established without pre-strain. The constitutive model of origin JC model was shown in Eq. 10.

$$\sigma = (A + B\varepsilon^{n})(1 + C\ln \dot{\varepsilon}^{*})(1 + T^{*m}) \tag{10}$$

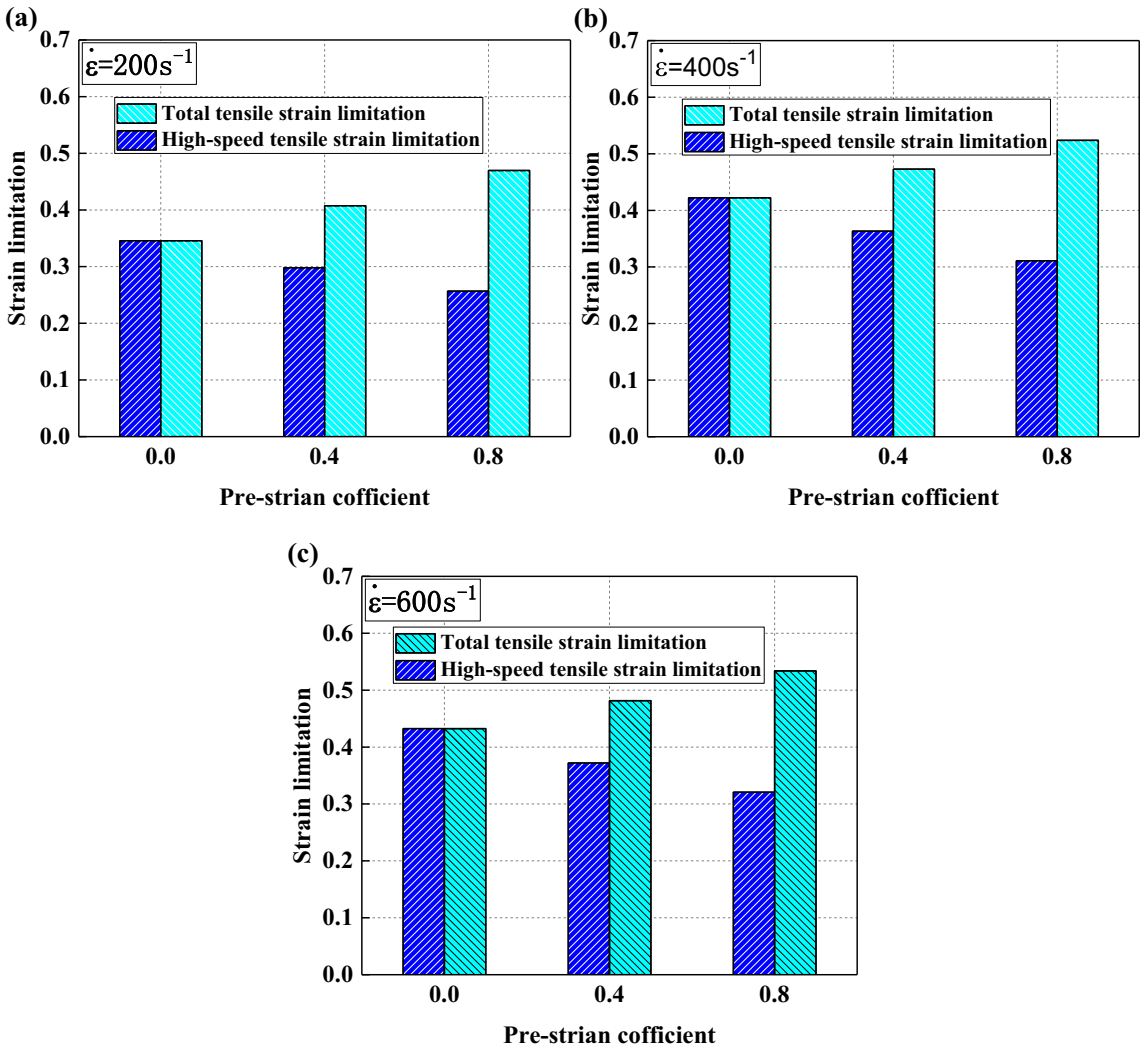

Fig. 7 Total tensile strain and high-speed tensile strain versus pre-strain percentage: (**a**) $\dot{\epsilon} = 200\ s^{-1}$, (**b**) $\dot{\epsilon} = 400\ s^{-1}$, (**c**) $\dot{\epsilon} = 600\ s^{-1}$

Where σ is flow stress, ε is the equivalent plastic strain, $\dot{\varepsilon}^* = \dot{\varepsilon}/\dot{\varepsilon}_0$ is the dimensionless plastic strain rate, $\dot{\epsilon}$ is the true strain rate, $\dot{\epsilon}_0$ is the reference strain rate, and T^{*m} is the homologous temperature. *A, B, n, C* and *m* are the material constants. $A + B\varepsilon^n$, $1 + C\ln\dot{\varepsilon}^*$ and $1 + T^{*m}$ are used to describe the work hardening effect, the strain rate effect, and the temperature effect, respectively.

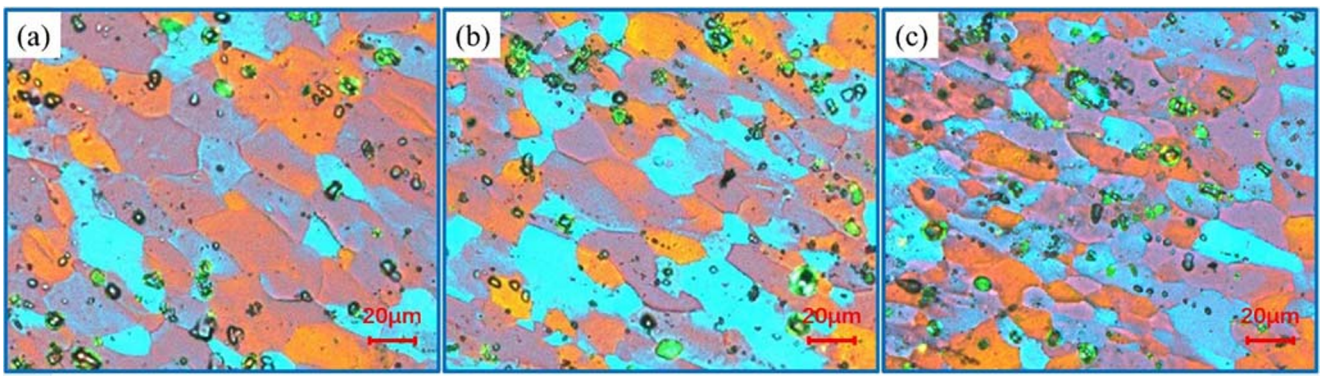

Fig. 8 Microscopic observation of grain size: (**a**) original sheet, (**b**) pure high-speed stretching condition, (**c**) high-speed stretching with 0.8 pre-strain coefficient condition

3.2.1 Determination of *A*, *B* and *n*

At the reference strain rate (0.001 s^{-1}), the JC model could be simplified to:

$$\sigma = A + B\varepsilon^n \tag{11}$$

The value of A in Eq. 11 was the yield stress (MPa) at reference temperature and reference strain rate. Based on the true stress-strain date under quasi-static stretching conditions, the value of A could be derived. Take logarithm operation on both sides of Eq. 11, and Eq. 11 was equivalent to Eq. 12:

$$\ln(\sigma - A) = \ln B + n \ln \varepsilon \tag{12}$$

Substituting the value of A and flow stress data at various strains into Eq. 12, a fitting line of $ln(\sigma - A)$ vs. $ln\epsilon$ was plotted. The value of B could be calculated from the intercept of the fitting line, and n was the slope.

3.2.2 Determination of *C*

The effect of temperature on flow stress could be eliminated, because the experiments were conducted at room temperature (reference temperature). Therefore, the JC model could be simplified to:

$$\sigma = (A + B\varepsilon^n)(1 + C \ln \dot{\varepsilon}^*) \tag{13}$$

Rearranging Eq. 13 to the following form:

$$\frac{\sigma}{A + B\varepsilon^n} - 1 = C \ln \frac{\dot{\varepsilon}}{0.001} \tag{14}$$

Because $A + B\epsilon^n$ is constant under a fixed strain, $\frac{\sigma}{A+B\sigma^n}$ is linearly related to $ln\frac{\dot{\epsilon}}{0.001}$. C was obtained from the slope of $\frac{\sigma}{A+B\sigma^n} - 1$ vs. $ln\frac{\dot{\epsilon}}{0.001}$ plot for a fixed strain at various strain rates. Since C was a constant in the JC model, the average of C at different strain was the final value of C.

The material constants of JC model for 6061-O aluminum alloy were given in Table 1. Using the parameters in Table 1, the comparisons between experimental flow stress values and predicted stress by JC model was shown in Fig. 9. Obviously, deviations between predicted and experimented results could be observed. The constitutive model should be improved for 6061-O aluminum alloy.

Table 1 Parameter of the Johnson-Cook model for AA6061-O

Parameter	*A* (MPa)	*B* (MPa)	*n*	*C*
value	63.44	479.42	0.72436	0.00673

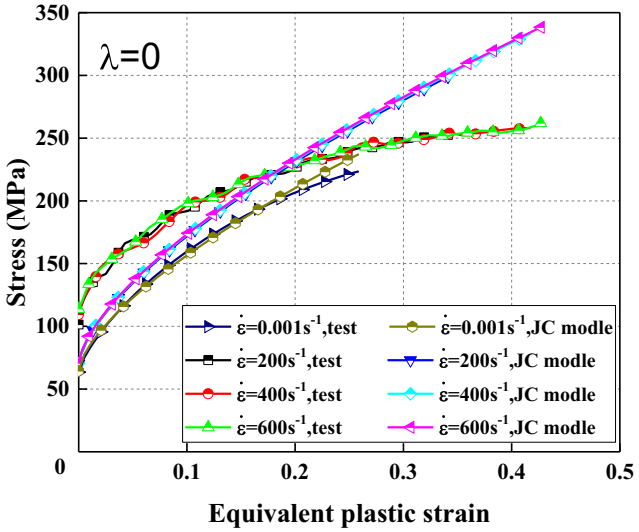

Fig. 9 Flow stress comparisons between the experiments and predicted result by J-C model when the pre-strain coefficient is zero

3.3 Modified Johnson-Cook model

The effects of strain, strain rate, and temperature on flow stress were mutually independent in the original JC model. However, the three influencing factors had new effects on flow stress [28]. In order to improve the accuracy of the constitutive model, many modified constitutive models had been proposed. In some previous research, the work hardening effect was a polynomial or exponential form about strain [29–32]; the coefficient of strain rate hardening was an equation for strain and strain rate [33].

The work hardening coefficient B in the original JC was a constant, which resulted in a bias between the experimental curve and the JC model curve as shown in Fig. 9. The coefficient of strain rate hardening was constant in the JC model and the effect of strain rate was shown in Eq. 15. Since A, B, ε, n, C, $\dot{\varepsilon}$ were positive, $\frac{\partial\sigma}{\partial\dot{\epsilon}}$ was also positive. Therefore, under the determined strain, the flow stress gradually increased as the strain rate increased. According to Fig. 3, the flow stress of the material increased with the increased of the pre-strain coefficient. It was believed that the effect of pre-strain on flow stress was about the function of pre-strain coefficient.

$$\frac{\partial\sigma}{\partial\dot{\varepsilon}} = (A + B\varepsilon^n) \cdot \frac{C}{\dot{\varepsilon}} > 0 \tag{15}$$

According to the above analysis, a modified JC constitutive model was established to describe the relationships between flow stress and strain, strain rate, pre-strain. The equation could be described as Eq. 16.

$$\sigma = [A + F(B) \cdot \varepsilon^n][1 + F(C) \cdot \ln \dot{\varepsilon}^*] \times [1 + F(D) \cdot \ln(1 + \lambda)] \tag{16}$$

Where $F(B)$ is the coefficient of strain hardening, $F(C)$ is the coefficient of strain-rate hardening, $F(D)$ is the coefficient of pre-strain hardening, λ is pre-strain coefficient. In Eq. 16, items $A + F(B) \bullet \epsilon^n$, $1 + F(C) \bullet \ln \dot{\epsilon}^*$ and $1 + F(D) \bullet \ln(1 + \lambda)$ were used to describe the work hardening effect, the strain rate effect, and the pre-strain effect, respectively.

3.3.1 Determination of the introduced *F* (*B*)

When the strain rate and pre-strain coefficient were 0.001 s^{-1} and 0, respectively, Eq. 16 could be expressed as follow:

$$\sigma = A + F(B) \cdot \varepsilon^n \tag{17}$$

As analyzed in Sect. 3.2, the true stress-strain curve of quasi-static tension deviated from the original JC model. This deviation was a function of the strain. Therefore, it was considered that $F(B)$ was an equation of strain, and the equation could be written as follows:

$$F(B) = B_1 \cdot \sin(B_2 \cdot \varepsilon + B_3) \tag{18}$$

where B_1, B_2 and B_3 are material constants. Based on the true stress-strain curve under quasi-static conditions, Eq. 18 was fitted by means of the regression analysis with the experimental results. According to the coefficients of the fitting formula, the values of A, B_1, B_2, B_3, and n were determined.

3.3.2 Determination of the introduced *F*(*C*)

Similarly, Eq. 16 could be simplified the following Eq. 19 when pre-strain coefficient was equal to zero.

$$\sigma = [A + F(B) \cdot \varepsilon^n][1 + F(C) \cdot \ln \dot{\varepsilon}^*] \tag{19}$$

The relationship between $F(C)$ and true strain ε was shown in Fig. 10. When the strain was zero, the $F(C)$ values at the strain rate of 200 s^{-1}, 400 s^{-1} and 600 s^{-1} were 0.0566, 0.0561, and 0.0597, respectively. However, when the strain was 0.3, the $F(C)$ values at the strain rate of 200 s^{-1}, 400 s^{-1} and 600 s^{-1} were 0.00514, 0.00517, and 0.00544, respectively. In addition, when the strain value was less than 0.12, the value of $F(C)$ decreased rapidly with the increase in strain, but when the strain was greater than 0.12, the value of $F(C)$ decreased slowly. Therefore, at small strains, the value of $F(C)$ was greatly affected by strain, and $F(C)$ approached a constant under a large strain.

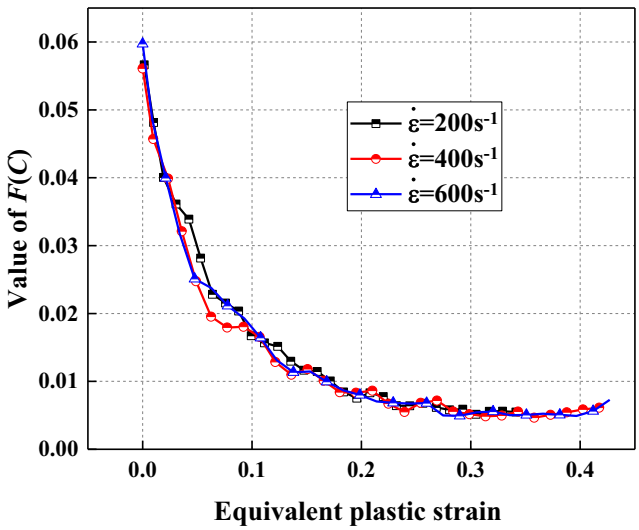

Fig. 10 Relationship between $F(C)$ and ε

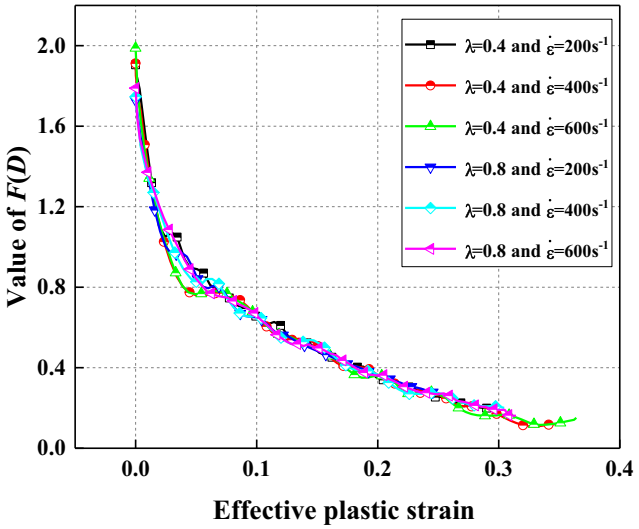

Fig. 11 Relationship between $F(D)$ and ε

The flow stress of the material was not much affected by the strain rate at the range of 200 s^{-1}-600 s^{-1}. Figure 10 also showed this trend that the value of $F(C)$ changed slightly at different strain rates. $F(C)$ was only the strain-dependent material parameter.

It was considered that the coefficient of strain rate hardening could be expressed as a function of strain and the function was suitable for different strain rates. The equation could be written as shown in Eq. 20

$$F(C) = C_1 + C_2 \cdot e^{C_3 \cdot \varepsilon} \tag{20}$$

where C_1, C_2 and C_3, are material constants. According to Eq. 20 and Fig. 10, the values of C_1, C_2, C_3, could be determined directly at the different strain rate. The final values of C_1, C_2 and C_3 were the average of the values of C_1, C_2 and C_3 at the different strain rate.

3.3.3 Determination of the introduced *F*(*D*)

Using the experimental flow stress data at different strains and Eq. 16, the relationship between $F(D)$ and true strain ε was shown in Fig. 11. At different strain rates and pre-strain coefficients, the trend of $F(D)$ with strain was the same, and it

Table 2 Parameters of the modified Johnson-Cook model for AA6061-O

Parameter	A (MPa)	B_1 (MPa)	B_2	B_3	n	C_1
value	63.44	1303.49	-0.52306	0.48103	0.75069	0.00534
Parameter	C_2	C_3	D_1	D_2	D_3	
value	0.04819	-15.16991	-0.25882	-0.38709	0.00476	

could be seen that a strain of 0.05 was the demarcation point of these curve trends.

It was considered that the coefficient of strain rate hardening could be expressed as a function of strain and the function was suitable for different strain rates. The equation could be written as shown in Eq. 21.

$$F(D) = D_1 + D_2 \cdot \ln(\varepsilon + D_3) \tag{21}$$

where D_1, D_2 and D_3, are material constants. According to Eq. 21 and Fig. 11, the final values of D_1, D_2 and D_3 could be determined directly by averaging the values of D_1, D_2 and D_3 at the different pre-strain coefficients and different strain rate.

The material constants of the modified JC model for AA6061-O aluminum alloy were given in Table 2.

The predicted values by modified JC model could be made according to Table 2 and Eq. 16. Comparisons between the experimental and predicted results by the modified JC model of AA6061-O aluminum alloy under three different high strain rates and three different pre-strain coefficients were shown in Fig. 12. It could be found that the modified JC model could give an accurate and precise estimate of the flow stress. Therefore, the modified JC model could be used in sheet metal forming simulations.

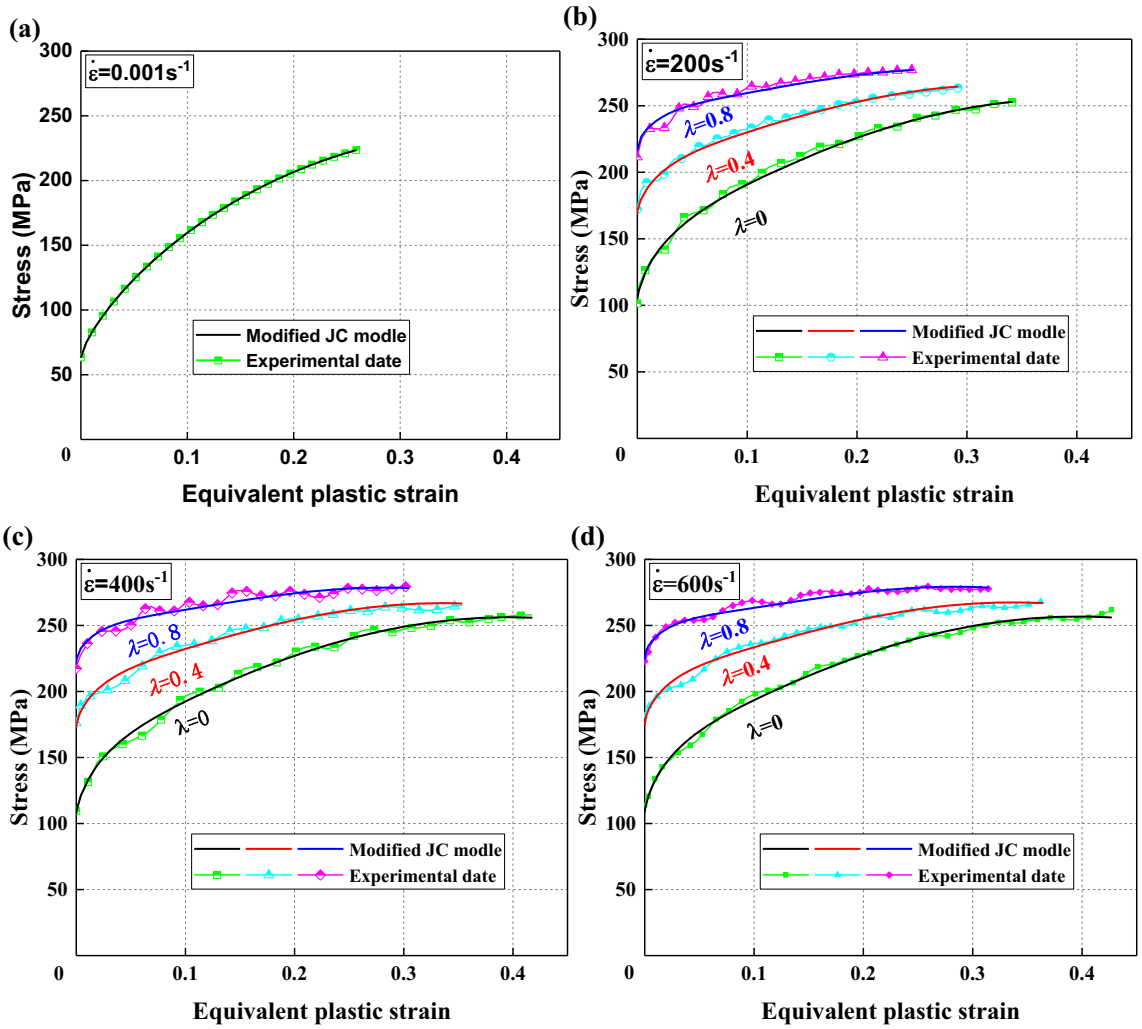

Fig. 12 Comparisons between predicted and experimental flow stress cures with different pre-strain coefficients

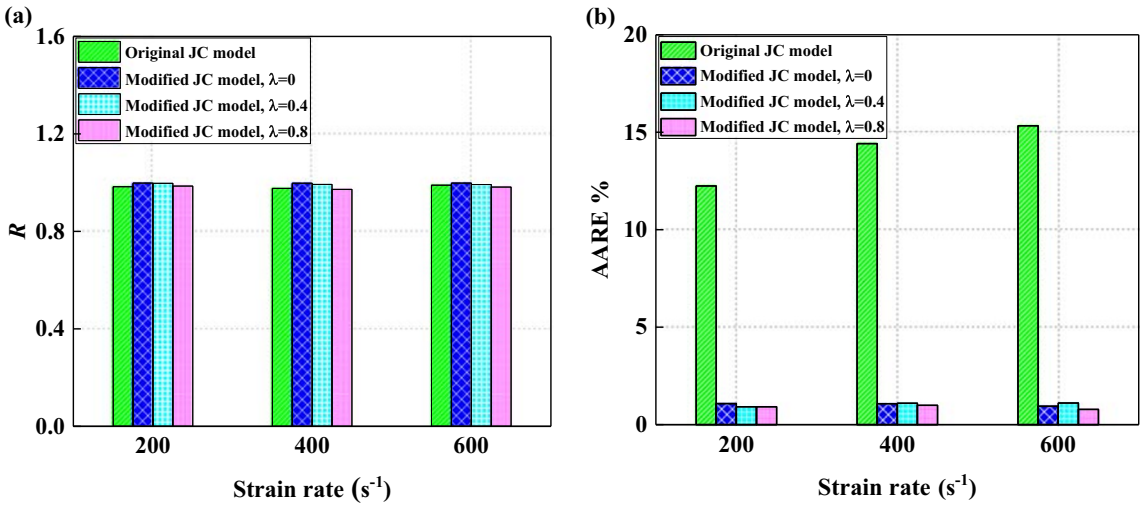

Fig. 13 Comparison of R and AARE between predicted values and experimental values of the two models: (**a**) R versus strain rate column graph, (**b**) AARE versus strain rate

In order to quantify the predictive ability of the modified JC model, the correlation coefficient (R) and average absolute relative error (AARE) were used. The correlation coefficient was the amount of linear correlation between experimental stresses and predicted flow stresses. The average absolute average error was used to evaluate the deviation of the predicted flow stresses from the experimental data. The R and AARE were expressed as:

$$R = \frac{\sum_{i=1}^{i=N}\left(\sigma_e^i - \overline{\sigma_e}\right)\left(\sigma_p^i - \overline{\sigma_p}\right)}{\sqrt{\sum_{i=1}^{i=N}\left(\sigma_e^i - \overline{\sigma_e}\right)^2 \sum_{i=1}^{i=N}\left(\sigma_p^i - \overline{\sigma_p}\right)^2}} \tag{22}$$

$$\mathrm{AARE} = \frac{1}{N}\sum_{i=1}^{i=N}\left|\frac{\sigma_e^i - \sigma_p^i}{\sigma_e^i}\right| \times 100\% \tag{23}$$

Where σ_e and $-\sigma_e$ are experimental true stress and the average values of experimental true stress, respectively. σ_p and $-\sigma_p$ are predicted true stress calculated by employing corresponding model and predicted true stress, respectively. N is the number of data employed in the investigations.

The calculated result of R and ARRE for the original JC model and modified JC model were shown in Fig. 13. The correlation coefficient for the original JC model and the modified JC model were greater than 0.97. The AARE coefficients of the original JC model and the modified JC model were quite different, and the improved model was close to zero. The comparison between the predictive values and the experimental values implied that the modified JC model was much more accurate than original JC model.

4. Validation of the numerical model

To verify the accuracy of the modified JC model, the commercial finite element code LS-DYNA was used to perform simulations of the dynamic test with a pre-strain coefficient of 0.4 and at a strain rate of 200 s^{-1}. The eight-node 3D element was used and the finite element model had 4000 elements with an

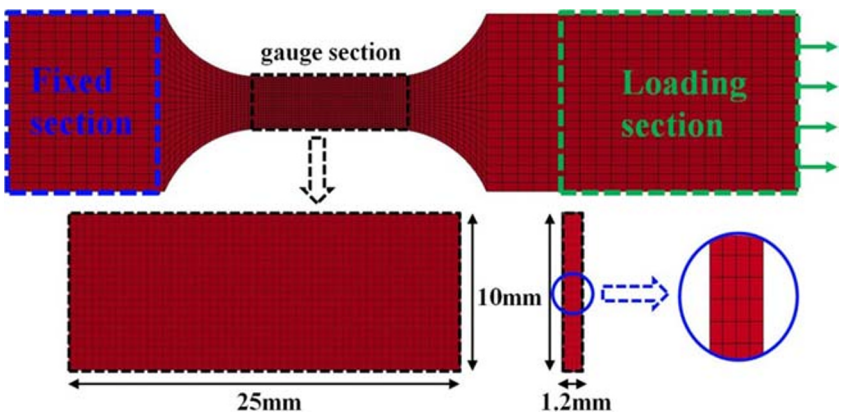

Fig. 14 Mesh in gauge section of finite element model

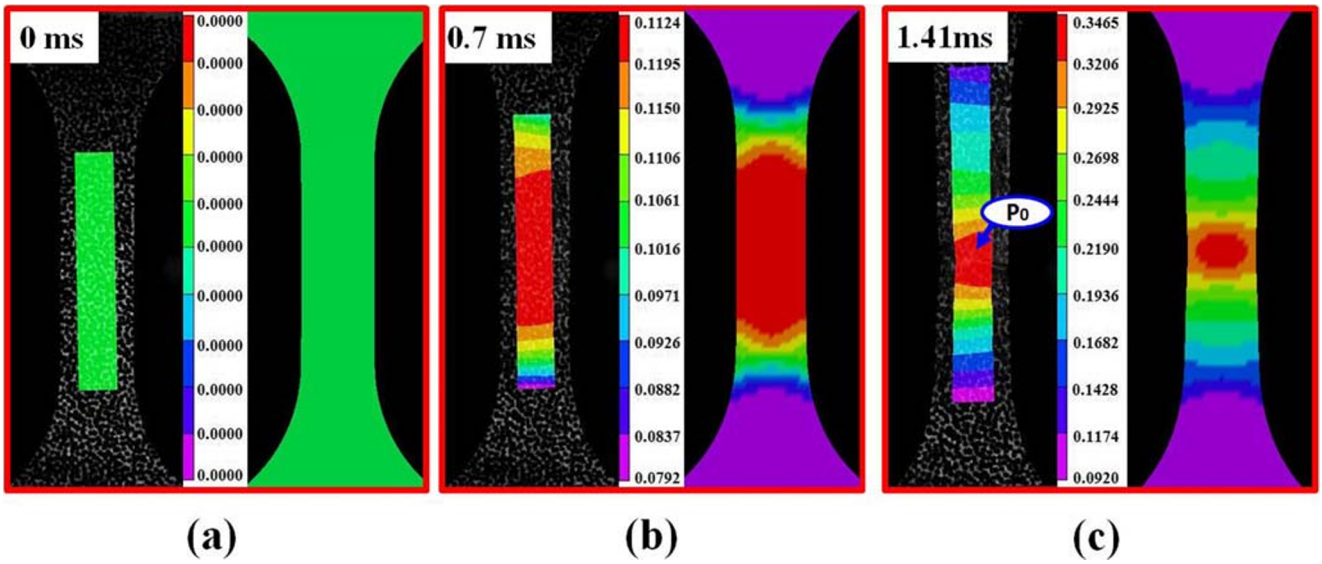

Fig. 15 Comparison of von-Mises Strain field distribution in the calculation area from DIC and numerical simulation at strain rate 200 s^{-1}, pre-strain coefficient 0.4: (**a**) t = 0 *ms*, (**b**) t = 0.5 *ms*, and (**c**) t = 1.02 *ms*

element size of 0.5 mm × 0.5 mm × 0.3 mm in the gauge section, as shown in Fig. 14

The model was first stretched to 2.879 mm under a displacement boundary. The simulations were performed using the modified JC model with strain rate of 0.001 s^{-1}. Then, the dynain file was derived from the calculation results. Finally, the model in the dynain file was redefined the material properties and the stretching velocity field. A speed boundary condition was implemented at the upper surface in the tensile specimen. The employed velocity was obtained from DIC technique. The modified JC model (pre-strain coefficient 0.4 and strain rate 200 s^{-1}) was applied in finite element simulation.

The comparison of the gauge section between the numerical simulation and the von-Mises strain field taken by DIC was shown in the Fig. 15. The results showed that the strain distributions of the DIC images and numerical simulations at different time were well matched. The stress-time curves comparison of simulation results and the DIC results near the fracture zone (Point P_0 in Fig. 15) was shown in Fig. 16. The numerical simulation showed good consistency with DIC measurement. The good agreements of simulation results and the DIC results confirmed the rationality of the proposed modified JC model.

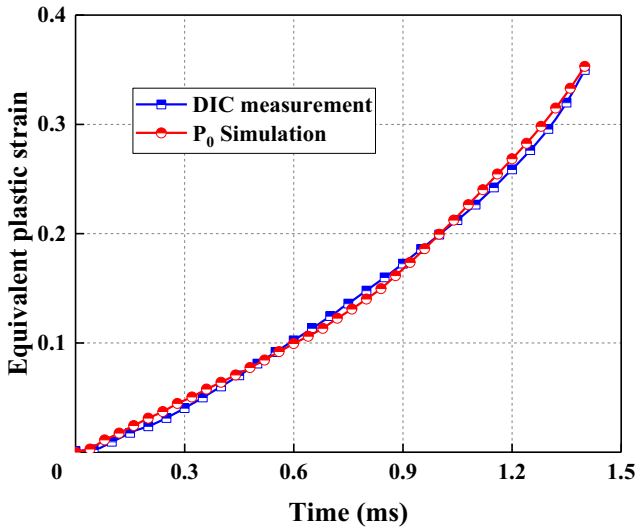

Fig. 16 Comparison of equivalent plastic strain-time curve of the calculation area from DIC measurement and numerical simulation near the region of fracture

5. Conclusions

In this paper, specimens of AA6061-O aluminum alloy with different pre-strain coefficients (0, 0.4 and 0.8) had been stretched at different strain rates (200 s^{-1}, 400 s^{-1} and 600 s^{-1}). Based on this study, the following conclusions could be drawn.

(1) Under the same pre-strain coefficient, the yield ratio was not sensitive to the strain rate of 200 s^{-1}-600 s^{-1}. However, the yield ratio could significantly increase with the increase of pre-strain coefficient, and the maximum yield ratio could be increased by 90.1%.

(2) The strain limitation of AA6061-O aluminum alloy was greatly affected by the pre-strain coefficient. The total tensile strain limitation increased as the pre-strain coefficient increased, and the maximum total tensile strain limitation increased by 35.9% compared with the pure high-speed tensile strain limitation.

(3) A modified JC model considering pre-strain coefficient was proposed. The modified model fitted well with experiments, and the max average absolute relative error was 1.108%.

Acknowledgement This project is supported by the National Natural Science Foundation of China (No. 51975202) and the Natural Science Foundation of Hunan Province (2019JJ30005), the National Key Research and Development Program of Hunan Province (2017GK2090).

Data availability The raw/processed data required to reproduce these findings cannot be shared at this time due to technical or time limitations.

Compliance with ethical standards

Conflict of Interest Conflict of Interest for all authors -None.

References

1. Seth M, Vohnout VJ, Daehn GS (2005) Formability of steel sheet in high velocity impact. J Mater Process Technol 168(3):390–400
2. Zia M, Fazli A, Soltanpour M (2017) Warm Electrohydraulic Forming: A Novel High Speed Forming Process. Procedia Eng 207:323–328
3. Ma H, Huang L, Wu M, Li J (2014) Dynamic Ductility and Fragmentation for Aluminum Alloy Using Electromagnetic Ring Expansion. Procedia Eng 81:787–792
4. Li G, Deng H, Mao Y, Zhang X, Cui J (2017) Study on AA5182 aluminum sheet formability using combined quasi-static-dynamic tensile processes. J Mater Process Technol 255:373–386
5. Choi MK, Huh H, Park N (2017) Process design of combined deep drawing and electromagnetic sharp edge forming of DP980 steel sheet. J Mater Process Technol 244:331–343
6. Fang J, Mo J, Li J (2017) Microstructure difference of 5052 aluminum alloys under conventional drawing and electromagnetic pulse assisted incremental drawing. Mater Charact 129:88–97
7. Shang J, Daehn G (2011) Electromagnetically assisted sheet metal stamping. J Mater Process Technol 211(5):868–874
8. Imbert J, Worswick M (2012) Reduction of a pre-formed radius in aluminium sheet using electromagnetic and conventional forming. J Mater Process Technol 212(9):1963–1972
9. Stiemer M, Unger J, Svendsen B, Blum H (2009) An arbitrary Lagrangian Eulerian approach to the three-dimensional simulation of electromagnetic forming. Comput Methods Appl Mech Eng 198(17):1535–1547
10. Luo W, Huang L, Li J, Liu X, Wang Z (2014) A novel multi-layer coil for a large and thick-walled component by electromagnetic forming. J Mater Process Technol 214(11):2811–2819
11. Bagheriasl R, Worswick M, Mckinley J, Simha H (2010) An effective warm forming process; numerical and experimental study. Int J Mater Form 3:219–222
12. Gao CY, Zhang LC (2012) Constitutive modelling of plasticity of fcc metals under extremely high strain rates. Int J Plasticity 32–33: 121–133
13. Lin YC, Li LT, Fu YX, Jiang YQ (2011) Hot compressive deformation behavior of 7075 Al alloy under elevated temperature. J Mater Sci 47(3):1306–1318
14. Lin YC, Chen XM, Liu G (2010) A modified Johnson–Cook model for tensile behaviors of typical high-strength alloy steel. Mater Sci Eng A 527(26):6980–6986
15. Samantaray D, Mandal S, Bhaduri AK (2009) A comparative study on Johnson Cook, modified Zerilli–Armstrong and Arrhenius-type constitutive models to predict elevated temperature flow behavior in modified 9Cr–1Mo steel. Comput Mater Sci 47(2):568–576
16. Zavinska O, Eijndhoven SJL, Claracq J, Doelder J (2010) Constitutive model parameters estimation from rheotens steady state and resonance characteristics. Int J Mater Form 1:807–810
17. Etaati A, Dehghani K, Ebrahimi GR, Wang H (2013) Predicting the flow stress behavior of Ni-42.5Ti-3Cu during hot deformation using constitutive equations. Met Mater Int 19(1):5–9
18. Slycken JV, Verleysen P, Degrieck J, Bouquerel J, De Cooman BC (2007) The effect of silicon, aluminium and phosphor on the dynamic behavior and phenomenological modelling of multiphase TRIP steels. Met Mater Int 13(2):93–101
19. Chen SR, Gray GT (1996) Constitutive behavior of tantalum and tantalum-tungsten alloys. Metall Mater Trans A 27(10):2994–3006
20. Zhao Y, Sun J, Li J, Yan Y, Wang P (2017) A comparative study on Johnson-Cook and modified Johnson-Cook constitutive material model to predict the dynamic behavior laser additive manufacturing FeCr alloy. J Alloy Compd 723:179–187
21. Jakus A, Fredenburg A, Thadhani N (2012) High-strain-rate behavior of maraging steel linear cellular alloys: Mechanical deformations. Mater Sci Eng A 534:452–458
22. Li HY, Li YH, Wang XF, Liu JJ, Wu Y (2013) A comparative study on modified Johnson Cook, modified Zerilli–Armstrong and Arrhenius-type constitutive models to predict the hot deformation behavior in 28CrMnMoV steel. Mater Des 49:493–501
23. Zhang DN, Shang guan QQ, Xie CJ, Liu F (2015) A modified Johnson–Cook model of dynamic tensile behaviors for 7075-T6 aluminum alloy. J Alloy Compd 619:186–194
24. Hou QY, Wang JT (2010) A modified Johnson–Cook constitutive model for Mg–Gd–Y alloy extended to a wide range of temperatures. Comput Mater Sci 50(1):147–152
25. Deng H, Mao Y, Li G, Cui J (2019) A study of electromagnetic free forming in AA5052 using digital image correlation method and FE analysis. J Manuf Process 37:595–605
26. Ou H, Yang Y, Hu M, Li G, Cui J (2019) Forming study on a tailor rolled blank (TRB) structure- formability evaluation and model verification. J Manuf Process 44:397–407
27. INTERNATIONAL STANDARD ISO 6892-1: 2009(E) Metallic Materials-Tensile testing-Part 1: Method of test at room temperature
28. Lin YC, Liu G (2010) A new mathematical model for predicting flow stress of typical high-strength alloy steel at elevated high temperature. Comput Mater Sci 48(1):54–58
29. Cai J, Wang K, Zhai P, Li F, Yang J (2014) A Modified Johnson-Cook Constitutive Equation to Predict Hot Deformation Behavior of Ti-6Al-4V Alloy. J Mater Eng Perform 24(1):32–44
30. He A, Xie G, Zhang H, Wang X (2013) A comparative study on Johnson–Cook, modified Johnson–Cook and Arrhenius-type constitutive models to predict the high temperature flow stress in 20CrMo alloy steel. Mater Des 52:677–685
31. Shokry A (2017) A Modified Johnson–Cook Model for Flow Behavior of Alloy 800H at Intermediate Strain Rates and High Temperatures. J Mater Eng Perform 26:5723–5730
32. Wang YP, Han Cj, Wang C, Li S (2010) A modified Johnson–Cook model for 30Cr2Ni4MoV rotor steel over a wide range of temperature and strain rate. J Mater Sci 46(9):2922–2927
33. Tan JQ, Zhan M, Liu S, Huang T, Guo J, Yang H (2015) A modified Johnson–Cook model for tensile flow behaviors of 7050-T7451 aluminum alloy at high strain rates. Mater Sci Eng A 631:214–219